CONF-9006220--5

UCRL-JC--104418

DE91 000404

PARTICLE DISTRIBUTIONS IN COLLISIONLESS MAGNETIC RECONNECTION: AN IMPLICIT PIC DESCRIPTION

Dennis W. Hewett
Gregory E. Francis
Claire E. Max

This paper was prepared for submittal to the XXVIII COSPAR, 1990, The Hague, The Netherlands, July 2-4, 1990.

June 29, 1990

Lawrence Livermore National Laboratory

DISCLAIMER

This document was prepared as an account of work sponsored by an agency of the United States Government. Neither the United States Government nor the University of California nor any of their employees, makes any warranty, express or implied, or assumes any legal liability or responsibility for the accuracy, completeness, or usefulness of any information, apparatus, product, or process disclosed, or represents that its use would not infringe privately owned rights. Reference herein to any specific commercial products, process, or service by trade name, trademark, manufacturer, or otherwise, does not necessarily constitute or imply its endorsement, recommendation, or favoring by the United States Government or the University of California. The views and opinions of authors expressed herein do not necessarily state or reflect those of the United States Government or the University of California, and shall not be used for advertising or product endorsement purposes.

Paper D2–July 3, 1990

Particle Distributions in Collisionless Magnetic Reconnection: An Implicit PIC Description

Dennis W. Hewett, Gregory E. Francis, and Claire E. Max

Institute of Geophysics and Planetary Physics
Lawrence Livermore National Laboratory
University of California

ABSTRACT

Evidence from magnetospheric and solar flare research supports the belief that collisionless magnetic reconnection can proceed on the Alfven-wave crossing timescale. Reconnection behavior that occurs this rapidly in collisionless plasmas is not well understood because underlying mechanisms depend on the details of the ion and electron distributions in the vicinity of the emerging X-points. We use the direct implicit Particle-In-Cell (PIC) code AVANTI to study the details of these distributions as they evolve in the self-consistent E and B fields of magnetic reconnection. We first consider a simple neutral sheet model. We observe rapid movement of the current-carrying electrons away from the emerging X-point. Later in time an oscillation of the trapped magnetic flux is found, superimposed upon continued linear growth due to plasma inflow at the ion sound speed. The addition of a current-aligned (east-west direction in the magnetosphere) and a normal (north-south in the magnetosphere) B field widen the scope of our studies.

I. INTRODUCTION

Magnetic reconnection has been invoked in the explanation of many physical situations in which magnetic topology changes are observed in electrically conductive media with some mechanism for dissipation. Such changes are commonly observed in astrophysical contexts, in magnetospheric physics, and in magnetic fusion research. Some sort of dissipation in the physical system is required, at least over a small region of time and space, or the conductive media and the magnetic field are locked together by the standard condition $\mathbf{E} = \mathbf{U}/c \times \mathbf{B}$. Changes in magnetic topology can occur only when $\mathbf{B}$ moves relative to the conductive medium. (See Parker 1979 for an overview of magnetic reconnection; Hones 1984 and Tajima 1989 for introductions to current research topics, and Schindler, Hesse, and Birn 1988 for a more general definition of magnetic field reconnection.) To relax the topology constraint we need only to generalize the equation for $\mathbf{E}$ using any of the additional terms available in the generalized momentum equation. Most often, a resistivity term, $\eta\mathbf{J}$ is added to the right-hand-side and the discussion shifts to what is termed "collisional" magnetic reconnection and models based on resistive fluid or MHD equations are used to understand the time behavior. Unfortunately the resistivity required to explain the observed reconnection rates in astrophysical or fusion contexts frequently requires values of η far in excess of any collision-based resistivity. Attempts to justify "anomalous" values for η based on saturation levels for various instabilities have not been very successful. Further, fluid or MHD representations of the conducting media have limitations due to low collisionality and the abrupt change in physics behavior as the scale lengths become on the order of the magnetic gyroradii. What is needed is a better model, one that includes particle kinetic effects. Particle-in-Cell or PIC simulation techniques are almost perfect for this task.

Kinetic Simulation of Magnetic Reconnection via PIC

Particle-In-Cell (PIC) models represent plasmas as an ensemble of "macro particles" that are advanced in time both position and velocity space, summed over velocities to find charge and current densities that are then used as source terms in Maxwell's equation to advance $\mathbf{E}$ and $\mathbf{B}$ to the next time level. Repeating this procedure provides a full description of the particle distributions and the self-consistent electromagnetic fields as they evolve in time. Details of this process can be found in several textbooks on plasma simulations (Hockney and Eastwood, 1988; Birdsall and Langdon, 1985; Tajima, 1989).

Although explicit PIC computer simulation techniques provide an adequate description of the micro-physics occurring in collisionless reconnection, stability requirements necessitate the use of very small timesteps (e.g. $\omega_{pe}\Delta t \leq 0.2$, where ω_{pe} is the electron plasma frequency, $\omega_{pe} = (4\pi n_e e^2/m_e)^{1/2}$). They therefore restrict affordable simulation parameters to artificially small ion-to-electron mass ratios (e.g. $m_i/m_e \approx 10$ to 25), and short temporal periods (LeBoeuf, Tajima, and Dawson 1982). In the present work, a new 2.5-D fully electromagnetic Direct Implicit PIC plasma simulation code AVANTI (Hewett and Langdon 1987) allows us to follow the dynamics of collisionless reconnection for realistic m_i/m_e, and for a factor of 2 to 3 longer time scales than have been simulated previously. Far more important advantages in this application are the model's elimination of the stability limit on time step due to light propagation, and the ability of this algorithm to properly model low frequency physics in a very noisy environment. This feature allows use of relatively high noise levels in simulations with far fewer particles per cell than other methods. Overall, we estimate that our implicit technique has expanded the parameter regime that can be studied by at least an order of magnitude.

Scope of this Reconnection Study

The subsequent four sections describe our simulation results. In Section II, we concentrate on the simple neutral-sheet geometry, using several ion to electron mass ratios. We first describe the initial state and then describe the simulation, noting that the initial stages of reconnection agree with predictions of linear tearing-mode theory. The nonlinear evolution of the process generates an intricate pattern of electric and magnetic fields about the emerging X-point that, when analyzed, give clues to underlying particle motion and, thus, insight into the details of the particle distributions. In Section III we consider our neutral-sheet geometry with the traditional neutral sheet model due to Harris. We give results for cases similar to those in Section II that show the two initializations are significantly different is some respects though their subsequent evolution seems to follow in familiar patterns. We compare results from these two initializations in Section IV. In Section V we generalise the neutral-sheet model by adding a zeroth-order magnetic field aligned with the current and we present preliminary results from our simulations of the open "magnetospheric" configuration first simulated by Zwingmann, at $m_i/m_e = 1$ and 200.

II. Simulations of the HFM Equilibrium

a. An Analytic Expression for the HFM Equilibrium

An initial equilibrium configuration can be constructed in a manner that allows very precise control of the ion profiles. By specifying the configuration of the ion distribution function, the electrons configuration can be determined as providing the densities and currents needed to hold this ion distribution in equilibrium. This procedure that we now outline is similar to a more general one by Hewett, Nielson and Winske (1976), and is exploited here to provide finite constant plasma density far from the neutral current sheet. We also specify that the ions carry no current, and thus are electrostatically confined. The ion temperature T_i is uniform.

We begin with an assumed ion distribution function that is Maxwellian in velocity, but with no ion drift:

$$f_i(z,\mathbf{v}) = (\frac{m_i}{2\pi T_i})^{3/2} n_i(z) exp\left\{-\frac{v_x^2+v_y^2+v_z^2}{2T_i}\right\} \tag{1}$$

where the functional form of the ion density $n_i(z)$ is as yet unspecified. The time-independent ion Vlasov equation reduces to

$$E_z(z) = \frac{-T_i}{q_i n_i}\frac{\partial n_i}{\partial z}, \tag{2}$$

a simple expression for the electric field needed to confine the ion pressure $n_i(z)T_i$. The origin of this field must lie in a small deviation from charge neutrality, given by inverting Gauss's equation

$$n_e(z) = n_i(z) - \frac{1}{4\pi e}\frac{\partial E_z}{\partial z}. \tag{3}$$

We use this equation to find the electron density profile $n_e(z)$ necessary to produce the ion-confining electrostatic field. Of course, only positive values of $n_e(z)$ are physical, and therefore care must be taken in choosing the appropriate ion profile $n_i(z)$. The ion density profile used in this work is:

$$n_i(z) = (n_{max} - n_{min})e^{-z^2/\delta^2} + n_{min}, \tag{4}$$

where n_{min} is large enough to ensure positive $n_e(z)$. We typically take n_{min} to be 25% of n_{max}.

The next step in constructing this equilibrium is to determine what magnetic field is required to confine the electron density profile, given the presence of the electrostatic field which confines the ions. We begin this step by assuming an electron distribution function similar to that given in Eq. (1), but with provisions for an electron drift in the y-direction that will be necessary to generate the electron-confining $B_x(z)$. The electron distribution has the form

$$f_e(z,\mathrm{v}) = (\frac{m_e}{2\pi T_e})^{3/2} n_e(z) exp\left\{-\frac{v_x^2 + (v_y - u_{ey}(z))^2 + v_z^2}{2T_e}\right\} \tag{5}$$

Again assuming that T_e is uniform, the electron Vlasov equation reduces to a relatively simple pressure balance relation

$$T_e \frac{\partial n_e}{\partial z} + q_e n_e (E_z + \frac{u_{ey} B_x}{c}) = 0 \tag{6}$$

Integrating in z we have

$$B_x^2(z) - B_x^2(z=\infty) = cT_i[n_i(z) - n_i(\infty)] + cT_e[n_e(z) - n_e(\infty)] \tag{7}$$

where we have used Ampere's law

$$u_{ey}(z) = \frac{c}{4\pi e n_e(z)} \frac{\partial B_x}{\partial z} \tag{8}$$

in the integration. Once we have obtained B_x from Eq. (7), we then use Eq. (8) to find the self-consistent electron drift.

Figure 1 shows plots of the relevant profiles for a typical equilibrium and its evolution. Before reconnection (Figure 1a), there is an initial magnetic field B_x which points in the negative x-direction for $z > 0$, and in the positive x-direction for $z < 0$. At $z = 0$ there is a "neutral sheet", a plane in which $B_x = 0$. The transition from $B_x < 0$ to $B_x > 0$ is sustained by a plasma current in the y-direction, which is assumed to be confined to a thin "sheath" region of width δ about $z = 0$.

After reconnection (Figure 1b), some field lines from above and below the neutral sheet have connected together to form one or more "X-points". In the regions between X-points lie "magnetic islands". These are closed structures enclosing so-called "O-points" on the original neutral plane. Figures 1 (b-d) show evolution of A_y, the magnetic flux–**B** vectors are everywhere tangent to these contours. We discuss the time evolution more completely below. It should be noted from Eq. (8) that the electron drift velocity $u_{ey}(z)$ in this equilibrium is a function of z, and that it is non-zero only in the neutral sheet region where $\partial B_x/\partial z \neq 0$. This characteristic of the equilibrium provides the numerical convenience of avoiding boundary condition difficulties for gyrating particle flow in the z direction at the simulation boundaries at $z = \pm L_z/2$.

b. Numerical Parameters

The simulation region for a typical simulation consists of a 40x96 z-x mesh, with all quantities initially uniform in x. The simulation box size is $L_z = 20c/\omega_{pe}$ in the z-direction and $L_x = 32c/\omega_{pe}$ in the x-direction. The initial neutral sheet width δ is $2c/\omega_{pe}$. Larmor radii for electrons and ions outside of the neutral sheet are $\rho_e = 0.4(m_i/2000m_e)^{1/2}c/\omega_{pe}$ and $\rho_i = 32(m/2000m_e)^{1/2}c/\omega_{pe}$, respectively. In these simulations, periodic boundary conditions are imposed at $x = 0$ and $x = L_x$. At $z = \pm L_z/2$, fields and particle densities approach values that are constant with respect to z, with perfect reflection boundary conditions for particles, Dirichlet zero conditions for $\mathbf{E}$, and Neumann zero conditions for $\mathbf{B}$.

We allow for anisotropy in electron temperatures parallel ($T_{e\parallel}$) and perpendicular ($T_{e\perp}$) to the initial magnetic field. Following the work of Chen and Palmadesso (1984), we use a cooler $T_{e\parallel}$ to trigger the initial stages of reconnection. The consequences of this anisotropy determine some properties of the typical particle orbits and will be discussed in a later section.

c. A Basic Description of Magnetic Reconnection

This rather simple neutral sheet configuration provides a useful example of the salient features of kinetic magnetic reconnection. Simulation particles are initialized with a weighted random number generator so that, in the limit of an infinite number of particles, the desired particle densities, currents, and temperatures are recovered.

A useful measure of reconnection is the amount of magnetic flux inside the separatrix. The separatrix is that contour of the current-aligned magnetic vector potential A_z that separates closed (reconnected) and open field lines. As can be readily seen in Fig. 1 (b-d), spontaneous reconnection occurs and coalescence of the early small scale island continues until there is only one magnetic island in the simulation region. As reconnection proceeds, we observe a build up of the electrostatic potential Φ, Fig. 2, signifying that more electrons than ions have moved away from the X-point into the vicinity of the O-point. These magnetized electrons have been driven towards the O-point and away from the X-point by a so-called "$\mathbf{E} \times \mathbf{B}$" drive. This force is primarily the result of an inductive current-aligned $\mathbf{E}$, shown in Fig. 3, interacting with the magnetic field in the $x-z$ plane. This electron current generates a self-consistent current-aligned $\mathbf{B}$ field that has the quadrupole structure shown in Fig. 4. Since the ions are unmagnetized they do not experience this $\mathbf{E} \times \mathbf{B}$ drive, and respond to the growing electrostatic potential on a time scale inversely proportional to their mass.

d. Electrostatic Ringing

Since the electrons are magnetized, their motion into the O-point can be expected to carry magnetic flux through the X-point into the O-point. This effect is responsible for the early rise in trapped flux shown in Fig. 5. Later in time we observe an oscillation in the trapped flux. Our interpretation (Hewett, Francis, Max 1988; Max, Francis, Hewett, in preparation) is that electrons are driven into the magnetic island more rapidly than the massive ions can follow, an electrostatic potential builds up at the O-point, and the electron flow is stopped and reversed until ion flow can be initiated to reduce the charge imbalance at the O-point. If simulations are run with an artificially small mass ratio, ($m_i/m_e \leq 100$), the ions can respond quickly to this attractive potential and the $\mathbf{E} \times \mathbf{B}$ drive then effectively continues to feed electrons and their associated magnetic flux into the O-point. Simulations with $m_i/m_e \geq 200$ not only have an oscillation in the trapped magnetic flux but also show oscillations in sign of the field-aligned B_y quadrupole (see Fig. 4).

The period of the electrostatic ringing is found to be independent of the ion parameters, and scales with the time required by a thermal electron to travel around a magnetic island in the x-z plane along the separatrix. Later in time an oscillation of the trapped magnetic flux through the O-point is found superimposed, upon continued linear growth due to the plasma inflow at the ion sound speed–the fastest time scale on which the ions can respond.

e. Particle Distributions for Reconnection in the HFM Equilibrium

We observe the rapid movement of the current-carrying electrons away from the emerging X-point towards the O-point. This effect has also been observed in laboratory reconnection experiments (Stenzel and Gekelman, 1979, 1981; Gekelman and Stenzel, 1979). Evidence from the particle phase space plots indicates that the fastest particles move out along the expanding separatrix. The evidence is found in the "wings" that develop in the v_y vs. z and v_y vs. x plots shown in Fig. 6.

Analysis of particle motions in these highly nonlinear configurations is difficult. As is apparent in Fig. 6, some regions of position space no longer have particles in certain regions of velocity space. Freezing fields and releasing test particles with some of these "lost" particle velocities confirm very high "mobilities" for these particles. One could easily conclude that these particles gain large amounts of energy through particle acceleration. However, identical runs with particles carried along in the self-consistently evolving fields did not show any unusual energy gains. Many if not most particles are gently removed from these "forbidden" regions well before the fields evolve to the magnitudes needed to give such large accelerations. Related work based on MHD simulations (Ambrosiano, *et. al.* 1988) suggests that only about 3% of the particles gain very much energy. Our results do not suggest no special clases of particles but rather a continous spectrum of energies. In Figure 6, we have evidence for these hot particles becoming localized at the O-points.

Other considerations provide evidence of appreciable particle energy gain from this process. Shown in Fig. 7 a) and b) are time histories of the total kinetic energy of electrons and ions, respectively. What is evident is that the electrons are being energized rapidly as the linear growth phase becomes nonlinear. The ions (in Fig. 7b) also gain energy but much later than the electrons. This energy peak is however not due to a very small fraction of the particles gaining a great deal of energy but, rather, a more substantial fraction of the particles "jetting" or moving from the X-point to the O-point as the reconnection rate grows.

We gain some insight by examining the types of orbits that make up the initial configurations, and later determine which of these types are **not** present in certain regions. The three possible orbit types are shown in Fig. 8. Fig. 8a) shows the dominant type of electron orbit in the current sheet: a typical betatron orbit. Betatron orbits are the predominant current carriers–having only negative velocities. Fig. 8b) shows the cycloidal orbit–the next most numerous type. Cycloidal orbits have positive velocities in the middle of the current sheet and negative velocities on the outside. Fig. 8c) shows a retrograde betatron orbit. These retrograde betatron orbits have the same velocity patterns as the cycloidal, though there are fewer of them because they require such a careful balance to continue skipping across the field null.

We also note that betatron orbits tend to concentrate current at the field null while the other two types of orbits tend to spread the current–they both decrease current on the inside of the current sheet and enhance the current on the outside. Loss of either cycloidal or retrograde betatron orbits has a tendency to cause the current sheet to narrow and thus further enhance the loss rate.

From our test particle studies, we are convinced that the particles with the largest negative v_y have betatron orbits. In fact the HFM configuration has virtually all betatron orbits in the initial current sheet. As reconnection progresses we find a high percentage of the current in the O-point to be carried by these particles. Test particles initiated with small magnitudes in v_y tend to have cycloidal orbits that accelerate towards the x-point along the separatrix. An interesting feature of these orbits is that as these cycloidal particles move along the separatrix, they move into the field null as they pass near the X-point. As they pass the X-point, they frequently change from cycloidal to retrograde betatron for one orbit as they skip across the field null.

Based on our observations of test particles, we speculate that cycloidal particles tend to gain x velocity until they make only one turn in the time required to move from X-point to X-point. Thus these particles can cross the field null at each X-point as a retrograde orbit particle. These speculations are difficult to make more concrete; considering the complex spatial and temporal behavior of the field aligned **E** and **B** fields in Figs. 3 and 4, ensemble orbit behavior remains a difficult numerical task.

III. Simulations of the Harris Equilibrium

The Harris equilibrium (Harris, 1962) is a similar analytic equilibrium to the HFM equilibrium we have just discussed; we consider it here for comparison with the results of our HFM studies. Both electrons and ions are drifting uniformly for all z in this equilibrium but the densities go to zero away from the current sheet. The drift velocities are such that the net current produces a magnetic field that confines both species. Because of this magnetic confinement, no confining electrostatic field is needed–leading to the analytic convenience of exact charge neutrality, $n_e(z) \equiv n_i(z)$.

The functional form for the density profiles are $n(z) = Nsech^2(z/\delta)$, where δ is the current sheet width, and are confined by magnetic fields of the form $B_x(z) = B_0 tanh(z/\delta)$. Details can be found in the original reference. The initial particle configuration is set up with the appropriate weight factors in a manner analogous that use for the HFM equilibrium.

The Harris equilibrium's response to PIC time integration is significantly different than the HFM response. The most apparent numerical disadvantage is that, for a given set of plasma parameters, reconnection proceeds more more slowly (by a factor of 3-5) for the Harris equilibrium. Indeed the reconnection proceeds so slowly that, even for $m_i/m_e > 200$, we observe no electrostatic ringing. Other differences are evident on closer inspection. In Fig. 9 we give the analogous phase space plots to those in Fig. 6 for the HFM case. In particular we note the movement, not of the current-carrying electrons but of the background electrons away from the emerging X-points–an apparent qualitative difference from the behavior using the HFM initial state.

of particles with positive or small magnitude v_y as a thinning of retrograde or cycloidal particles that did not exist in the HFM equilibrium initially. (Remember that the all of the phase space plots shown here are sums across the **entire** simulation.) Particles in both equilibria tend to migrate away from the X-point due to magnetic curvature. In the HFM equilibrium, gyrating particles with no net flow are driven into the X-point from external regions to replenish the distribution lost from the X-point. With the Harris equilibrium, there are no particles to be brought in because the external density is zero.

IV. Particle Distributions: A Comparison Between Harris and HFM Initializations

We now discuss the observed particle distribution functions for these two types of initialization. It is easier to evaluate the contribution of the various types of particle orbits in the more dynamic HFM equilibrium initialized simulations. Consider the three orbit types in the $\mathbf{E}$ and $\mathbf{B}$ field configurations shown in Figs. 3 and 4. Due to the temperature anisotropy in the initialization, we have amplified the factors in particle behavior that most strongly affect reconnection in two ways. First, the particle orbits have oscillations that are predominately in the $y-z$ plane. At the X-point, all three types see curvature in the $\mathbf{B}$ field that tends to move them towards the O-point. Simply, we have enhanced the "magnetic moment" of the average particle due to the anisotropic initialization, increasing their tendency to move away from regions of converging field lines. Second, we have reduced the x-velocity of the average particle and thus have reduced the stabilizing effect of particles streaming along the field null. Rapid streaming along the field null diffuses the coherent behavior needed to allow "gathering" of particles in an O-point.

Since the betatron orbits are the most energetic, we expect these particles to be among the first to move away from the emerging X-point. By the time the configuration has undergone significant reconnection, the v_y vs z and v_y vs x phase space plots in Fig. 6 reveal that indeed these betatron particles (the ones with the largest negative v_y values) have moved to the O-points.

As the betatron particles leave the X-point, electrons from the exterior move in to fill the void. (These particles do not exist in the Harris equilibrium–$n_e = n_i = 0$ in this region.) These particles are predominately cycloidal; in the exterior regions far from the neutral sheet, they had only the thermal energy and were simply gyrating about the external B_x field. As they fill the X-point and are $\mathbf{E} \times \mathbf{B}$ driven out towards the O-point, they move out along the separatrix as cycloidal orbits and finally simply gyrate about a sepratrix as the ∇B drift goes to zero for large z. Since there is a modestly increasing E_y experienced by the electrons, on average the particles will lose energy–the positive v_y part of the orbit being nearer to $z = 0$ and experiencing a stronger deceleration than can be recovered on the opposite side of the orbit. This cooling can be see in Fig. 6 in which we shown the v_z vs z phase space that exhibits a cooler temperature just outside of the neutral sheet region.

There are very few particles with retrograde betatron orbits in either equilibrium. Some can develop as the external cycloidal particles get forced into the X-point where they sometimes skip across the field null and begin to execute cycloidal orbits on the opposite side. We have in fact observed carefully-initialized test particles that execute cycloidal motion along the separatrix on alternate sides of successive O-points as they translate down the system in the x-direction.

We believe the orbital dynamics in the Harris-initialized simulations are similar to what we have just described, though the lack of a large number of strong betatron orbits and their dynamics strongly curtails the rate at which reconnection occurs. A well-known way to increase the growth rate is to start with a drift velocity that is greater than the thermal velocity. This will provide a greater fraction of initial particles to have betatron orbits and, for reasons similar to those applied to the HFM equilibrium, we expect the reconnection rate to increase.

V. Simulations of Geometries with Additional Components of B

a. Simulations of the HFM Equilibrium with Shear

There are several ways to generalize the studies we have just described. Both the HFM and the Harris geometry can be generalized by adding additional zeroth-order components of magnetic field to the initial configuration. If one includes a magnetic component in the y-direction (out of the paper in Figure 1), then the starting configuration represents a sheared magnetic field; at the plane $z = 0$, only one component of the field vanishes ($B_x = 0$). We have added such a current-aligned field to our HFM equilibrium. This (magnetospheric east-west) magnetic field, if sufficiently strong, magnetizes electrons even in the neutral sheet. If this field is above a threshold, a new diamagnetic electron flow around the O-point results from additional $\mathbf{E} \times \mathbf{B}$ drifts. Many aspects are qualitatively similar to the previous case and will be discussed in a forthcoming paper (Max, Francis, and Hewett, in preparation).

b. Simulations with Normal B field: the Birn Equilibrium

Another way to generalize our simulation geometry is to include an initial magnetic field component normal to the neutral sheet. In the coordinate system used here, this would be a component of the initial magnetic field in the z-direction, as shown in Fig. 10a. For example, this geometry exists in planetary magnetotails, where the normal **B** field component is due to the inherent dipole field of the planet. Because the dipole strength decreases with distance from the planet, the initial magnetic field configuration is under tension: $(\partial/\partial x)(B_z^2/8\pi)$ is not equal to zero. Once reconnection has occurred, this magnetic tension is released and the magnetic islands are ejected outwards with considerable kinetic energy, forming so-called "plasmoids" (Figure 10b). Plasmoid structures have been observed in the earth's magnetotail following the onset of energetic reconnection events (Hones et al. 1984).

Zwingmann (1989) has used the equilibrium of Birn (1989) to model this configuration with zeroth-order field normal to the current sheet. We have used a similar initialization and, to date, have verified the qualitative aspects found by Zwingman with $m_i = m_e$–the contours of A_y are shown in Fig. 10b. Since this is an equilibrium based on a uniform shift of all species types in each local area, we are not suprised that this configuration exhibits the "thinning" of the slower particles in the v_y vs. x phase plots shown in Fig. 11a since, as with the Harris equilibrium, there are no "external" particles to fill in the phase space at an emerging X-point.

We see few qualitative differences from this picture as we increase $m_i/m_e = 200$. Since the electrons are magnetised even at the field null, we might expect this mode to be the ion rather than electron tearing mode and we would then expect an increase in the time for reconnection to occur, as indicated by the greater time required for comprable behavior in diagnostics. Our prelimenary results also indicate that as the mass ratio increases, the number of O-points that develop also increases–contrary to the expected behavior from simple ion tearing.

ACKNOWLEDGEMENTS

The authors gratefully acknowledge helpful discussions with Dr. J. Büchner of the Central Institute for Astrophysics in Potsdam, GDR and Dr. L.M. Zelenyi of the Space Research Institute in Moscow.

This research was performed under the auspices of the U.S. Department of Energy by the Lawrence Livermore National Laboratory under contract No. W-7405-ENG-48.

References

[1] Ambrosiano, J., Matthaeus, W.H., Goldstein, M., Plante, D. 1988, *J. Geophys. Res.*, 93, 14383.

[2] Birdsall, C.K. and Langdon A.B. 1985, *Plasma Physics via Computer Simulation* (New York: McGraw-Hill).

[3] Birn, J. 1979, *J. Geophys. Res.*, **84**, 5143.

[4] Chen, J. and Palmadessc, P. 1984, *Phys. Fluids*, **27**, 1198.

[5] Gekelman, W. and Stenzel, R.L. 1981, *J. Geophys. Res.*, **86**, 659.

[6] Harris, E.G. 1962, *Nuovo Cimento*, **23**, 115.

[7] Hewett, D.W., Francis, G.E., and Max, C.E. 1988, *Phys. Rev. Lett.*, **61**, 893.

[8] Hewett, D.W., Nielson, and Winske, D. 1976, *Phys. Fluids*, **19**, 443.

[9] Hewett, D.W. and Langdon, A.B. 1987, *J. Comp. Phys.*, **72**, 121.

[10] Hockney, R.W., and Eastwood, J.W. 1988, *Computer Simulation Using Particles* (Bristol: Adam Hilger).

[11] Hones, E.W. Jr. 1984, *Magnetic Reconnection in Space and Laboratory Plasmas* (Washington DC: American Geophysical Union).

[12] Hones, E.W. Jr., Baker, D.N., Bame, S.J., Feldman, W.C., Gosling, J.T., McCmoas, D.J., Zwickl, R.D., Slavin, J. Smith, E.J., and Tsurutani, B.T. 1984, *Geophys. Res. Letters*, **11**, 5.

[13] Leboeuf, J.N., Tajima, T., and Dawson, J.M. 1982, *Phys. Fluids*, **25**, 784.

[14] Max, C.E., Francis, G.E., and Hewett, D.W. 1990, in preparation, *Ap. J.*.

[15] Parker, E.N. 1979, *Cosmical Magnetic Fields* (Oxford: Clarendon Press), chapter 15.

[16] Schindler, K., Hesse, M., and Birn, J. 1988, *J. Geophys. Res.*, **93**, 5547.

[17] Stenzel, R.L. and Gekelman, W. 1981, *J. Geophys. Res.*, **86**, 649.

[18] Stenzel, R.L. and Gekelman, W. 1979, *Phys. Rev. Lett.*, **42**, 1055.

[19] Tajima, T. 1989, *Computational Plasma Physics* (New York: Addison Wesley), chapter 14.

[20] Zwingman, W. 1989, *Reconnection in Space Plasma, Vol. II* (Paris: European Space Agency), 67.

Figure Captions

Figure 1. a) Profiles of initial electrostatic field E_x (dashed) and magnetic field B_y (solid) across the neutral sheet for the HFM equilibrium. Both fields have units of $m_e c\omega_{pe0}/e$. The sheet current in the y-direction is carried by electrons. Ions are contained by the electrostatic field. The initially uniform electron and ion temperatures are $T_{e\perp}/m_e c^2 = 2.8 \times 10^{-2}$, $T_{e\parallel} = (4/9)T_{e\perp}$, $T_i/m_e c^2 = 8.0 \times 10^{-2}$. (b-d): Magnetic flux contours (solid) and separatrix (dotted) in x-z plane: (b) At $t = 30\omega_{pe}^{-1}$, showing small-scale electron-driven filaments; (c) At $t = 160\omega_{pe}^{-1}$, as coalescence begins; (d) At $t = 410\omega_{pe}^{-1}$, with only one X-point remaining.

Figure 2. Contours of the electrostatic potential Φ for the simulation shown in Fig. 1 at time t=250 ω_{pe}^{-1}. The negative value of Φ in the O-point region is caused by an excess of electrons.

Figure 3. Contours of the current-aligned inductive electric field E_y for the simulation shown in Fig. 1 at time t=250 ω_{pe}^{-1}. The positive value of E_y in the X-point region provides the $\mathbf{E} \times \mathbf{B}$ electron drive in to the O-point.

Figure 4. Contours of the current-aligned magnetic field B_y for the simulation shown in Fig. 1 at time t=250 ω_{pe}^{-1}. The quadrupole spatial behavior results from an electron flow into through the X-point into the O-point. Later the electron flow will reverse, changing the sign of both this field and the inductive E_y.

Figure 5. Trapped flux vs time for a representative simulation run. The electron and ion temperatures are as given in Fig. 1a, and $m_i/m_e = 2000$.

Figure 6. Electron phase space plots for the run shown in Fig. 1 at t=250 ω_{pe}^{-1}. Shown are a) the v_y vs z and b) v_y vs x phase spaces averaged over all x and z, respectively. Note the absence of fast current-carrying electrons in a) in the region of the X-point–the current carriers are the first to leave the region of an emerging X-point. Further note the appearance of an apparent double-valued distribution near the edge of the sheet current that, upon correlation of a) and b), can be recognized as cycloidal particles moving out along the separatrix.

Figure 7. Evidence for both a) electron and b) ion jetting are found in the time histories of the x-directed kinetic energies.

Figure 8. Schematic plots of the three basic orbit types. a) shows a typical betatron orbit, the dominant type of electron orbit in the current sheet. Betatron orbits are the predominant current carriers–having only negative velocities. b) shows the cycloidal orbit–the next most numerous type. Cycloidal orbits have positive velocities in the middle and negative velocities on the outside. Retrograde betatron orbits c) have similar velocity patterns but occur relatively infrequently because few particles have the careful balance of parameters to continue skipping across the field null.

Figure 9. Electron phase space plots for a Harris equilibrium run with similar parameters to the HFM run shown in Fig. 1. The Harris equilibrium reconnects much more slowly than the HFM equilibrium–the time here is t=1250 ω_{pe}^{-1}. Shown are a) the v_y vs z and b) v_y vs x phase spaces averaged over all x and z, respectively. We note the movement, not of the current-carrying electrons as in Fig. 6, but of the background electrons away from the emerging X-points–an apparent qualitative difference now explained by the lack of particles in the "exterior" region to repopulate the X-point.

Figure 10. Schematic representation of the Birn configuration. In a) is the initial configuration shown by contours of A_y and in b) are typical simulations results for simulations with $m_i/m_e = 1$ after t=450 ω_{pe}^{-1} that show the formation of two "plasmoids". In c) is the corresponding simulation with $m_i/m_e = 200$ after t=2400 ω_{pe}^{-1} that show the formation of three or more "plasmoids".

Figure 11. The corresponding particle distributions a) and z-averaged charge density ρ for the simulation shown in Fig. 10b with $m_i/m_e = 1$ have the characteristic thinning of the small magnitude and positive v_y velocities characteristic of the Harris equilibrium. The corresponding result for $m_i/m_e = 200$ is shown in b) in which a greater number of O-points are evident.

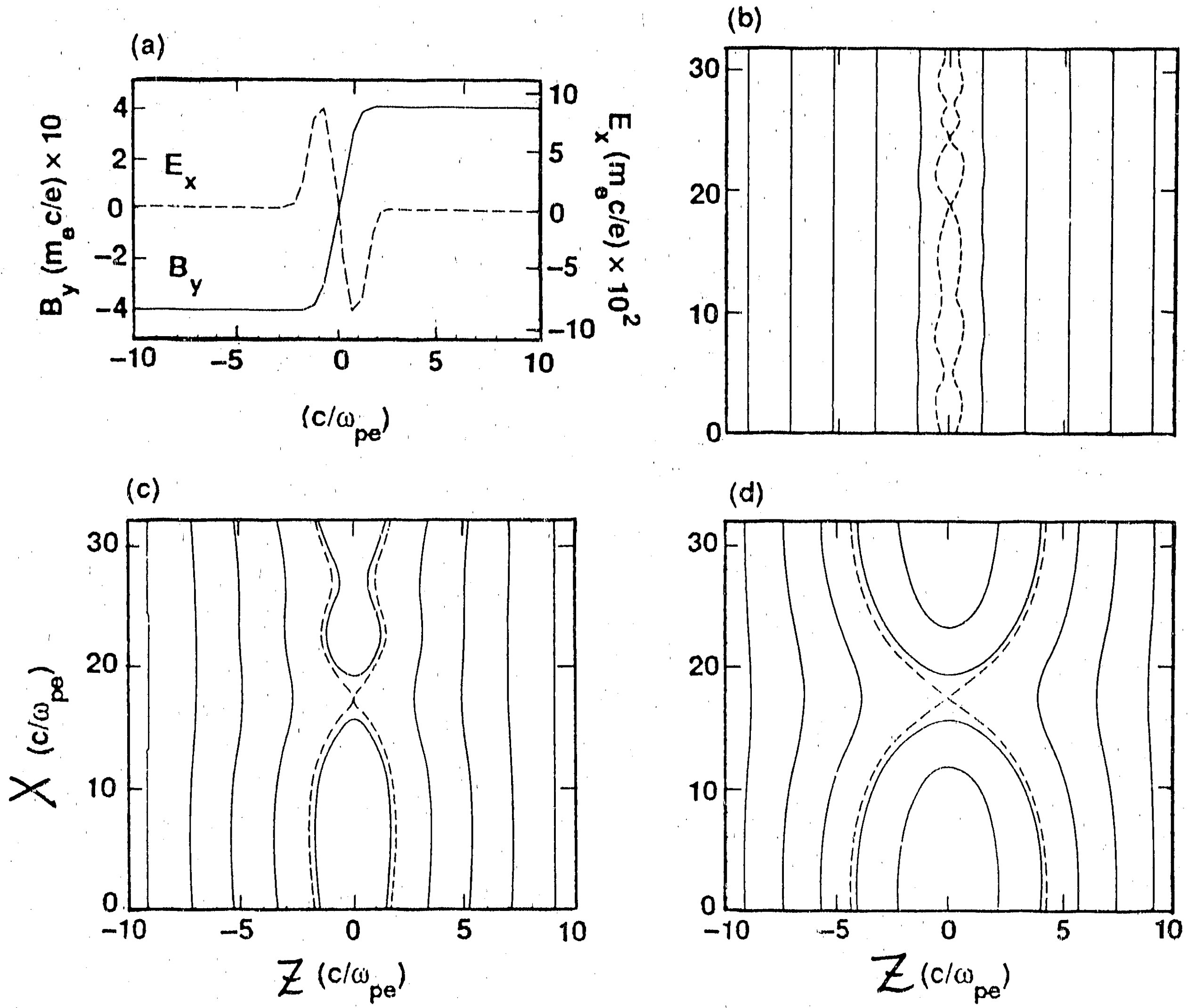

(a)
(b)
(c)
(d)
B_y $(m_e c/e) \times 10$
E_x $(m_e c/e) \times 10^2$
E_x
B_y
(c/ω_{pe})
X (c/ω_{pe})
Z (c/ω_{pe})
Z (c/ω_{pe})

Fig. 1

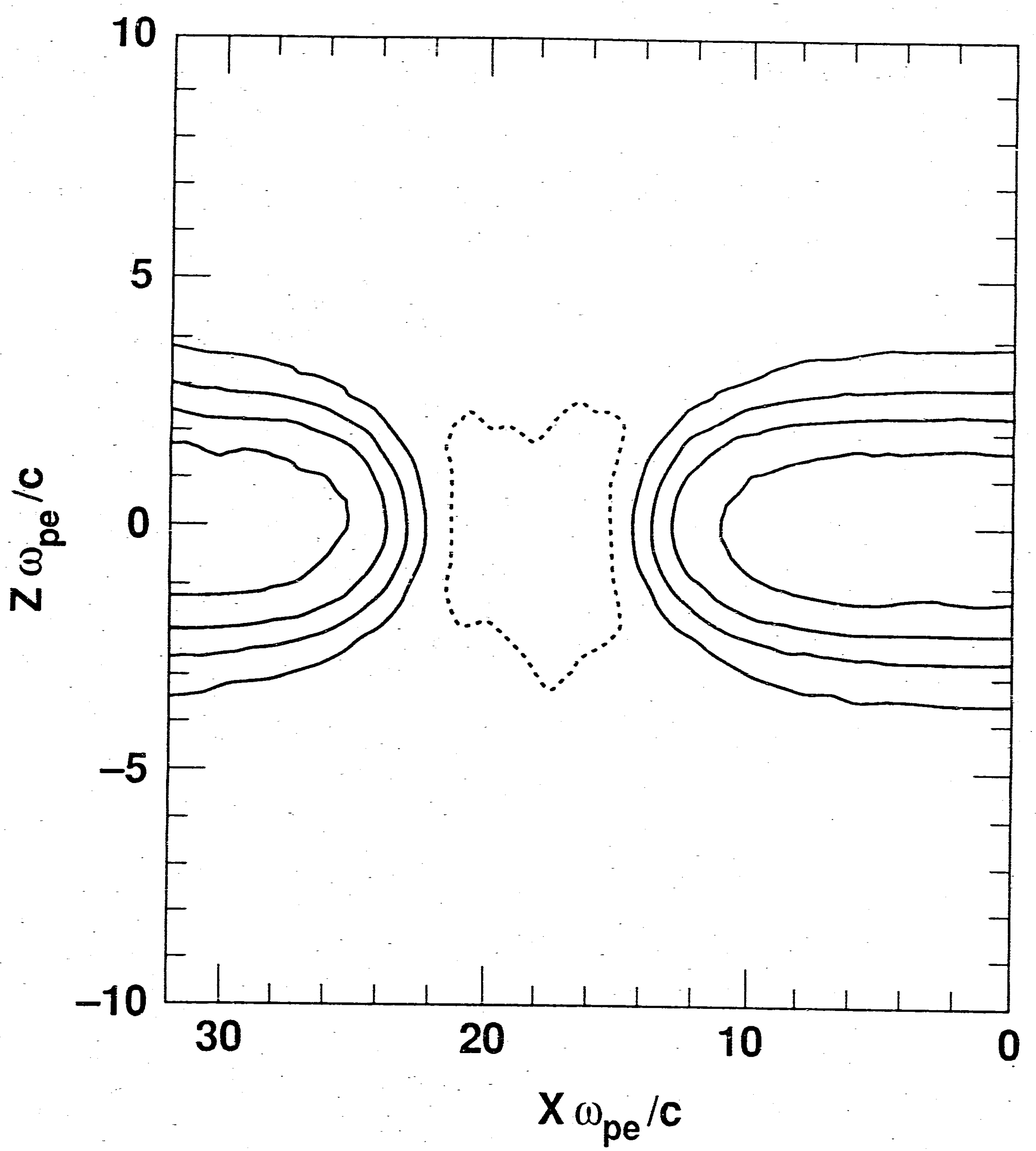

BE-U-11601-2(vgc)

Fig. 2

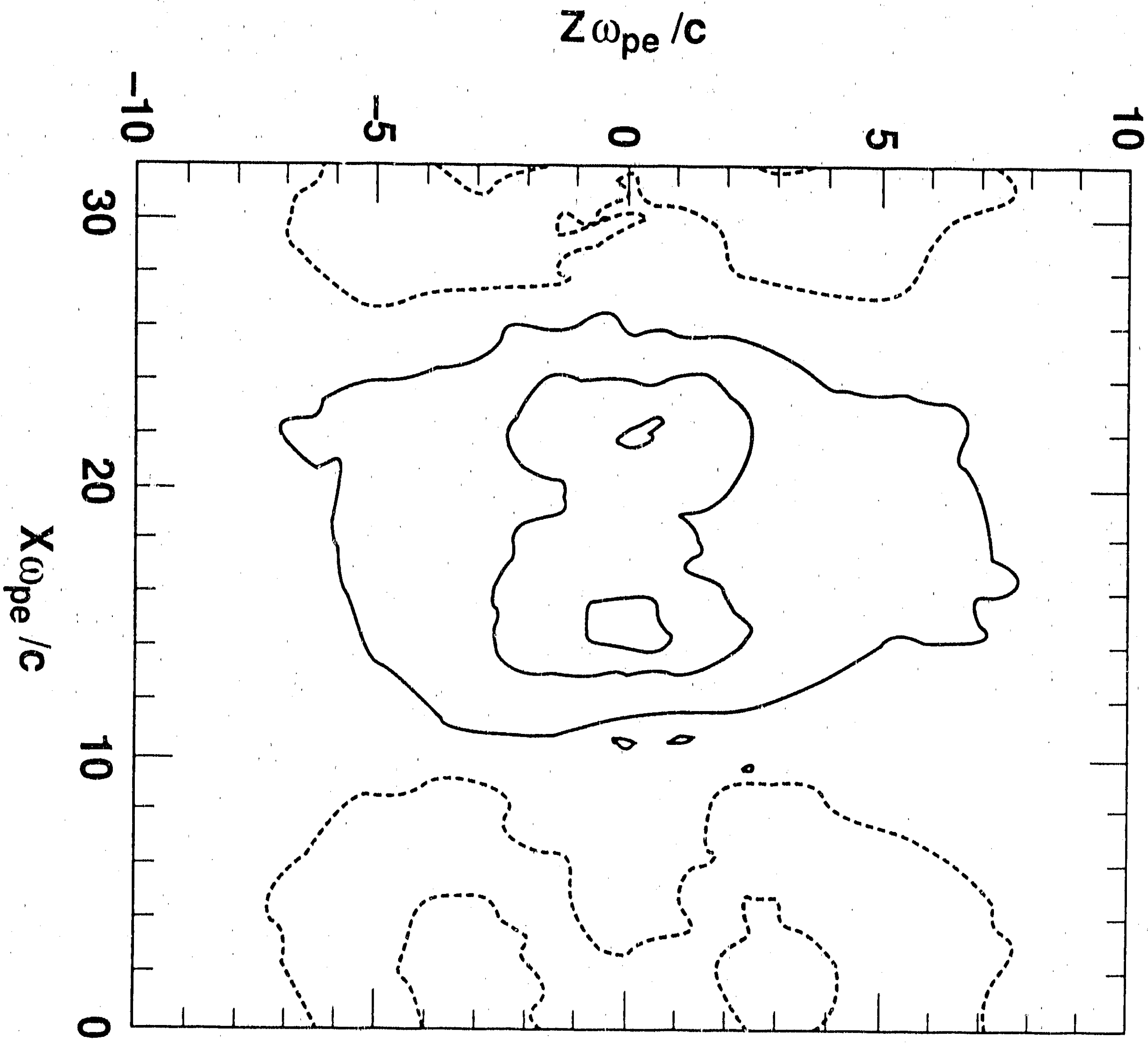

Fig. 3

BE-U-11601-2(vgb)

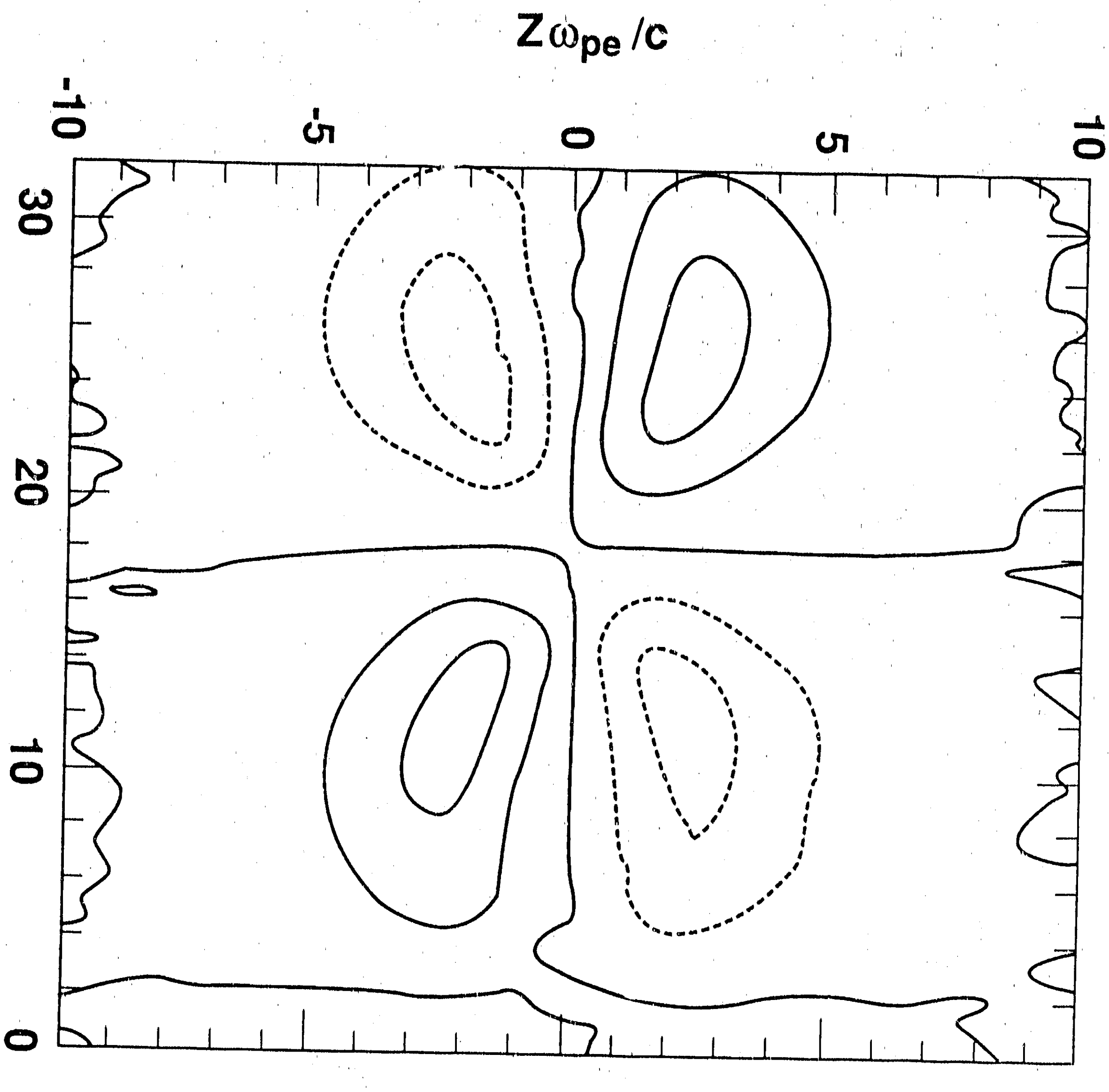

Fig. 4

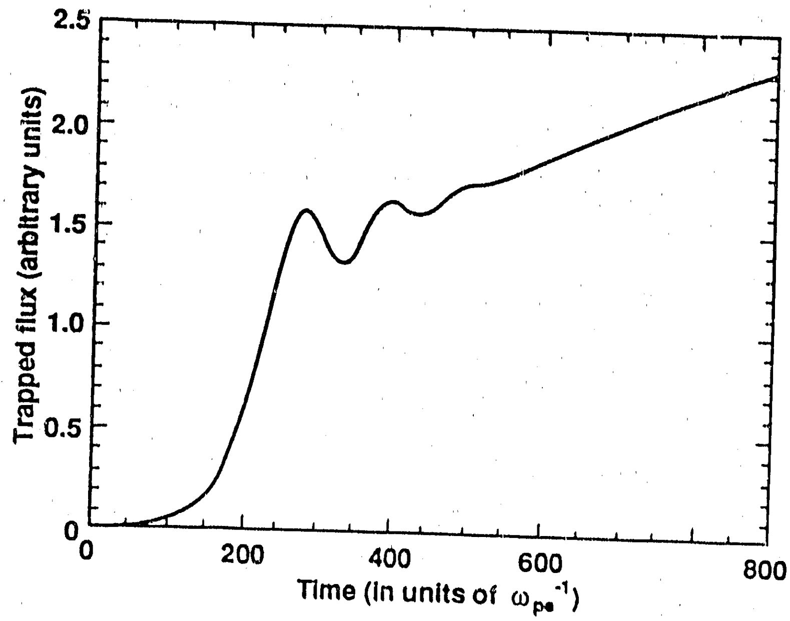

Figure 5

PT-AS17-U-10810-3

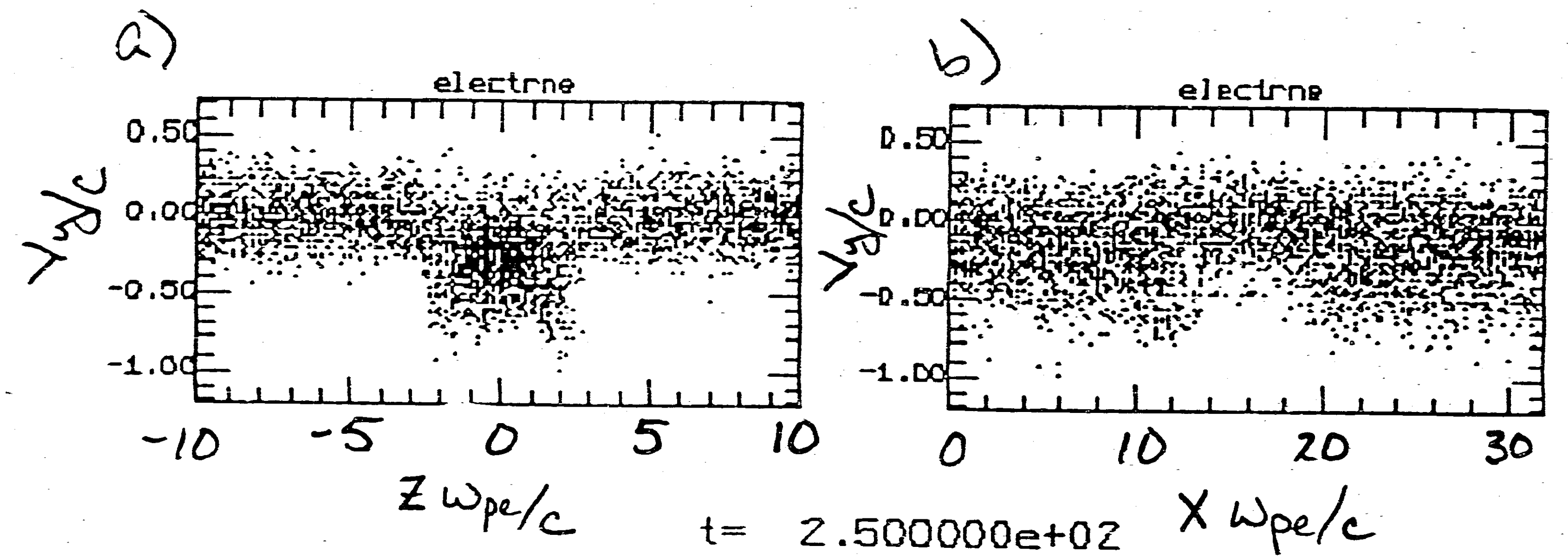

a)
electrne
V_y/c
0.50
0.00
-0.50
-1.00
-10
-5
0
5
10
$Z\,\omega_{pe}/c$
b)
electrne
V_y/c
0.50
0.00
-0.50
-1.00
0
10
20
30
$X\,\omega_{pe}/c$
t= 2.500000e+02

Fig. 6

a) electron directed energy

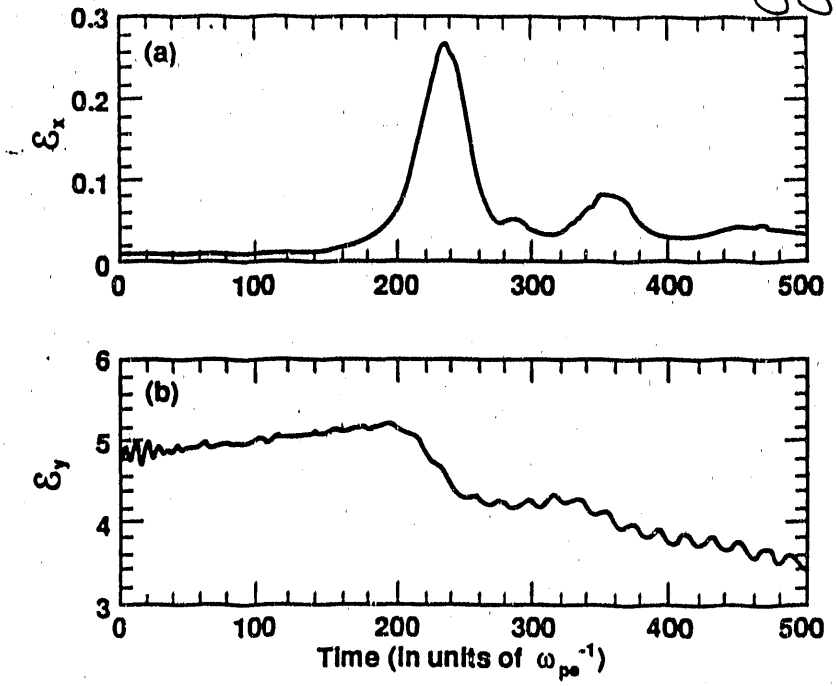

b) ion directed energy

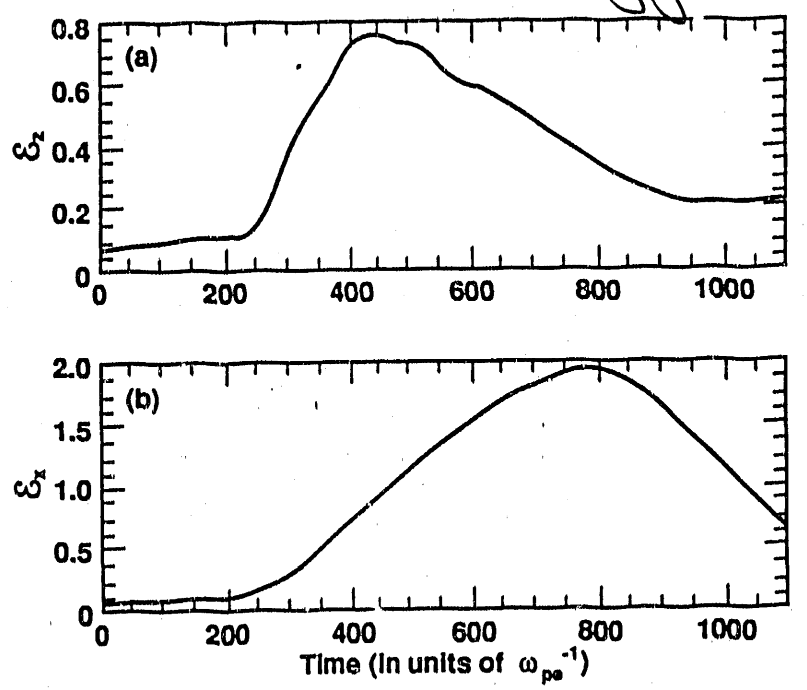

Fig. 7

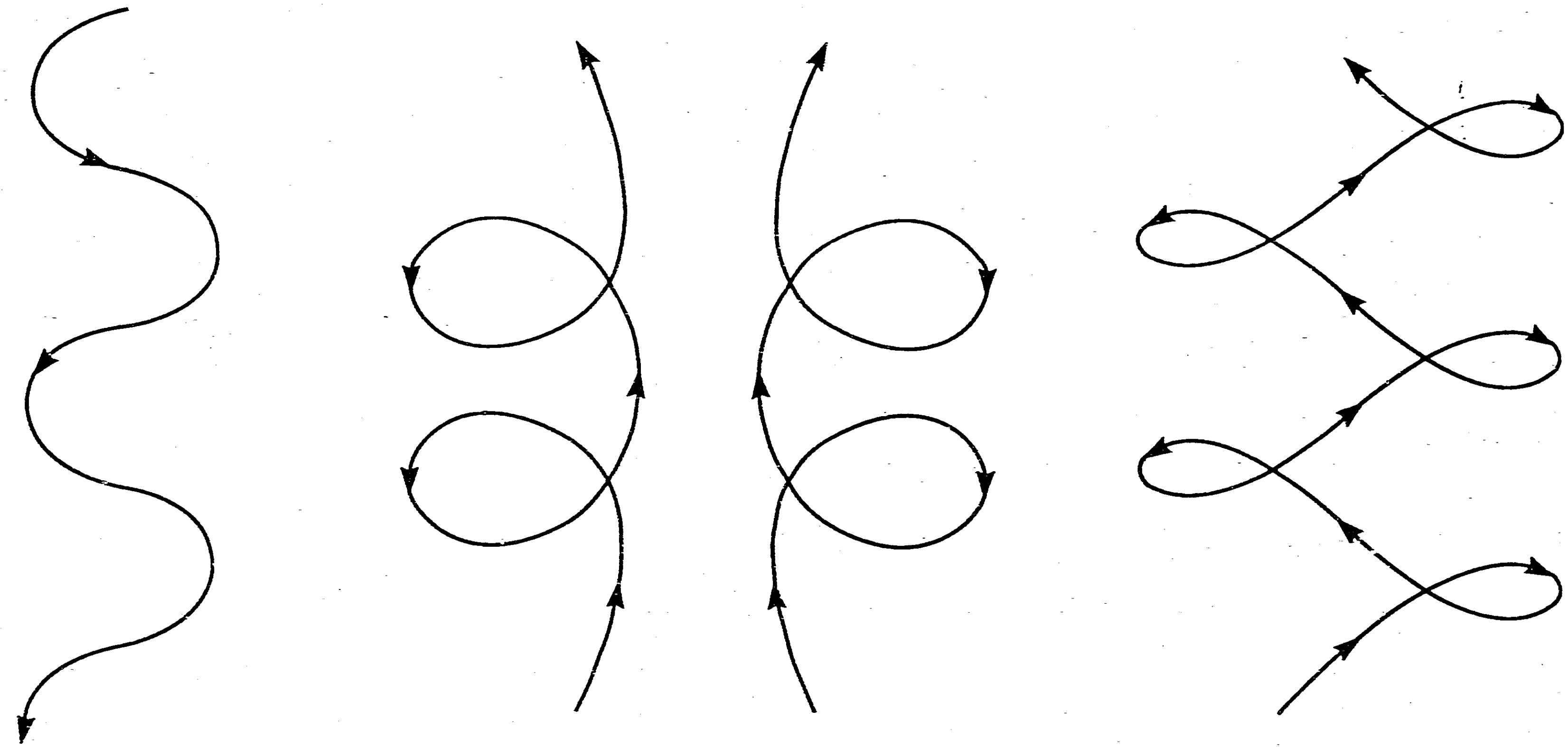

Betatron Cycloidal Retrograde Betatron

PT-S127-U-11601-2

Fig. 8

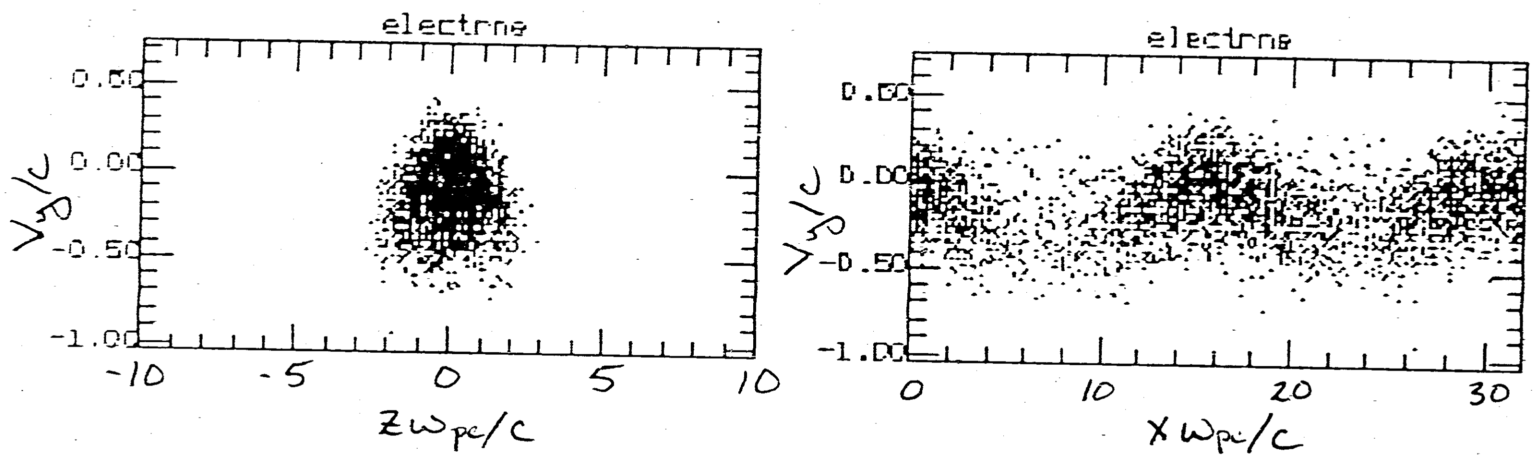
electrns
0.50
0.00
-0.50
-1.00
-10
-5
0
5
10
V_y/c
$z\omega_{pe}/c$
electrns
0.50
0.00
-0.50
-1.00
0
10
20
30
V_y/c
$x\omega_{pe}/c$

Fig. 9

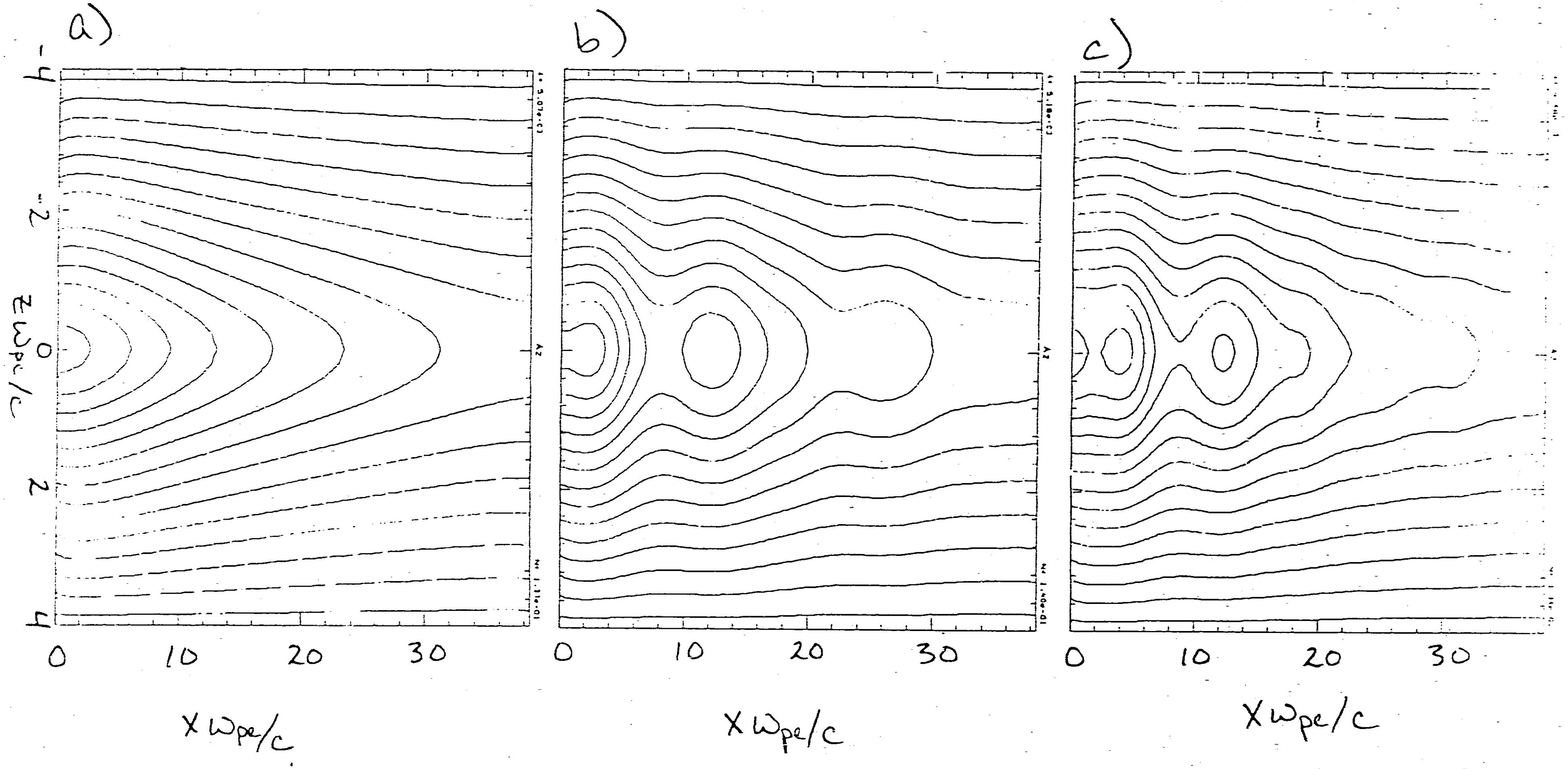

Fig. 10

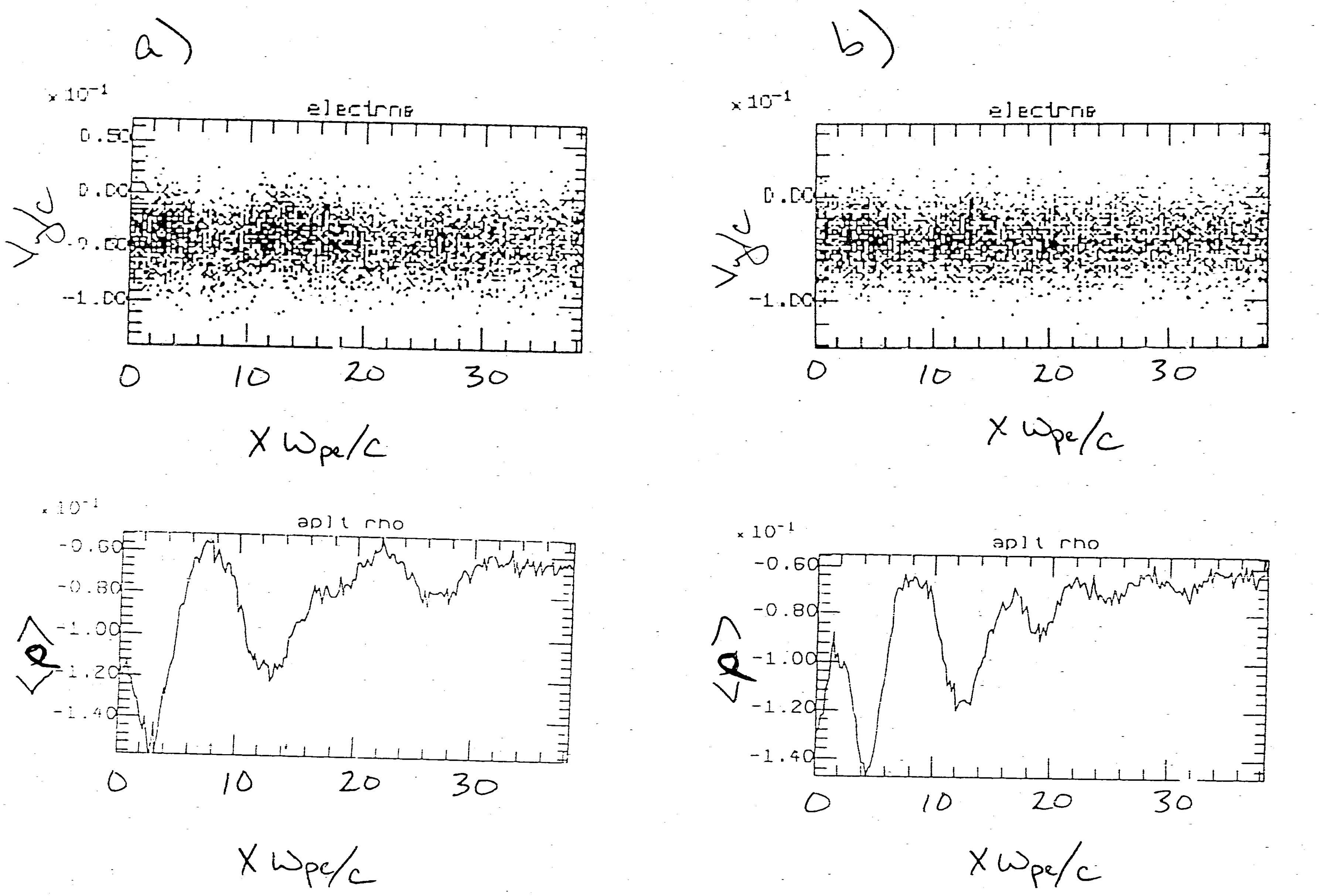
a)
b)
electrns
apl t rho
$\times 10^{-1}$
V_y/c
$\langle\rho\rangle$
0
10
20
30
X ω_{pe}/c

Fig. 11

END

DATE FILMED

10 / 23 / 90